Comparison of binary black hole initial data sets

Vijay Varma,[1] Mark A. Scheel,[1] and Harald P. Pfeiffer[2,3]

[1] *Theoretical Astrophysics 350-17, California Institute of Technology, Pasadena, CA 91125, USA*
[2] *Albert-Einstein-Institut, Max-Planck-Institut fr Gravitationsphysik, D-14476 Potsdam-Golm, Germany*
[3] *Canadian Institute for Theoretical Astrophysics, 60 St. George Street, University of Toronto, Toronto, ON M5S 3H8, Canada*

(Dated: November 15, 2018)

We present improvements to construction of binary black hole initial data used in SpEC (the Spectral Einstein Code). We introduce new boundary conditions for the extended conformal thin sandwich elliptic equations that enforce the excision surfaces to be slightly inside rather than on the apparent horizons, thus avoiding extrapolation into the black holes at the last stage of initial data construction. We find that this improves initial data constraint violations near and inside the apparent horizons by about 3 orders of magnitude. We construct several initial data sets that are intended to be astrophysically equivalent but use different free data, boundary conditions, and initial gauge conditions. These include free data chosen as a superposition of two black holes in time-independent horizon-penetrating harmonic and damped harmonic coordinates. We also implement initial data for which the initial gauge satisfies the harmonic and damped harmonic gauge conditions; this can be done independently of the free data, since this amounts to a choice of the time derivatives of the lapse and shift. We compare these initial data sets by evolving them. We show that the gravitational waveforms extracted during the evolution of these different initial data sets agree very well after excluding initial transients. However, we do find small differences between these waveforms, which we attribute to small differences in initial orbital eccentricity, and in initial BH masses and spins, resulting from the different choices of free data. Among the cases considered, we find that superposed harmonic initial data leads to significantly smaller transients, smaller variation in BH spins and masses during these transients, smaller constraint violations, and more computationally efficient evolutions. Finally, we study the impact of initial data choices on the construction of zero-eccentricity initial data.

I. INTRODUCTION

Numerical simulations of binary black holes (BBH) have been crucial for our understanding of BBH systems. For example, these simulations are important for the construction of accurate waveform models that cover the inspiral-merger-ringdown phases of a BBH system [1–5]; these models were used in successful detections [6–10] of gravitational waves by LIGO [11]. Accurate waveform models are necessary not only for the detection of gravitational wave signals but also for making inferences about the astrophysical properties of the sources [12] and for conducting strong field tests of general relativity [13].

A numerical BBH simulation begins with the construction of initial data that describes the state of the system on some three-dimensional initial surface labeled $t = 0$. Constructing initial data requires not only solving the Einstein constraint equations, but also freely choosing the initial spatial coordinates, the embedding of the three-dimensional initial surface in the four-dimensional spacetime, and some physical degrees of freedom; these choices are encoded in freely-specifiable functions and boundary conditions that are used in the solution of the constraint equations. The subset of these choices that amount to choosing coordinates should not, of course, affect the physics [14], but they may affect the robustness and accuracy of the subsequent evolution. This is because they influence the gauge degrees of freedom that evolve along with, and are intermixed with, the physical degrees of freedom.

In this paper we study how binary black hole simulations are affected by different choices of free data, gauge, and boundary conditions that are made when constructing initial data sets that are meant to be physically identical. We consider simulations performed with one particular numerical relativity code, the Spectral Einstein Code (SpEC) [15].

A. Summary of initial data for SpEC simulations

Before discussing how to improve the treatment of initial data, we first outline the current procedure used to construct initial data for binary black hole simulations using SpEC; this procedure is described in more detail in Sec. II. We adopt the Extended Conformal Thin Sandwich (XCTS) formalism [16, 17], and the free data supplied to the XCTS equations are chosen to be constructed from a superposition of two single black holes (BHs) in Kerr-Schild coordinates [18]. The region inside each of the BHs is excised from the computational domain, and boundary conditions are chosen that enforce the boundaries of these excision regions to be apparent horizons [19].

After the XCTS system of equations is solved, yielding a constraint-satisfying initial data set, the metric quantities are interpolated (and extrapolated) onto a new numerical grid that extends slightly inside the original excision boundaries. This new grid is used for the evolution. On the new grid the apparent horizons lie inside the computational domain rather than on its boundary, and this

allows the subsequent evolution to track the apparent horizons as they dynamically change in shape and size. Unfortunately, the small extrapolation to points inside the apparent horizons introduces some constraint violations in the vicinity of the excision boundaries.

Binary black hole initial data described above represent a physical solution to Einstein's equations but do not result in an exact snapshot of a quasi-equilibrium inspiral: the solution contains near-zone transient dynamics and does not include the correct initial gravitational radiation in the far zone. During evolution the system relaxes into a quasi-equilibrium state with the mismatch radiating away as a pulse of spurious radiation, which is generally referred to as *junk radiation*. The initial transients typically contain high spatial and temporal frequencies, so that resolving them is computationally expensive. For this reason, we typically choose not to fully resolve them at all, and we instead simply discard the initial part of the gravitational waveforms that are affected by these transients.

In addition to initial data, evolution also requires an initial choice of gauge. SpEC employs the generalized harmonic formulation of the Einstein equations [20–23], where gauge conditions are imposed through gauge source functions H_a (see II C). At the beginning of a binary black hole simulation, H_a is currently chosen such that the time derivatives of lapse and shift vanish at $t = 0$ in a frame co-rotating with the binary; this quasi-equilibrium condition is intended to minimize gauge dynamics at the beginning of the evolution [24]. However, a different choice of H_a, the *damped harmonic* gauge [25–27], is usually necessary later in the evolution when the black holes merge. The choice of H_a cannot be discontinuous in time because time derivatives of H_a appear in the evolution equations. Hence, a smooth gauge transformation is applied in the early stages of evolution to move into damped harmonic gauge.

B. Improvements in initial data treatment

In this paper we present several improvements to BBH initial data construction. First, we introduce new boundary conditions for the XCTS elliptic equations that enforce the excision surfaces to have a negative expansion. This means that the excision surfaces are already inside the apparent horizons, eliminating the need to extrapolate inside the horizons during the initial data construction. We find that this improves constraint violations in initial data near and inside the apparent horizon surfaces by about 3 orders of magnitude.

Next, we construct several initial data sets that implement different free data in the XCTS equations as well as different initial gauge conditions. The new free data choices include superpositions of two single BHs in time-independent horizon-penetrating harmonic [28] and damped harmonic [29] coordinates rather than in Kerr-Schild coordinates. The new initial gauge choices include imposing (to numerical truncation error) the harmonic and damped harmonic gauge conditions at $t = 0$, instead of setting the initial time derivatives of the lapse and shift to zero.

We evolve all these initial data sets. Among all the initial data constructions considered here, we find that superposed harmonic initial data exhibits the most favorable behavior in subsequent evolutions. Superposed harmonic initial data exhibits the smallest amount of junk radiation, and the smallest variation in the measured masses and spins of the BHs during the initial relaxation. Furthermore, the constraint violations during the initial relaxation are smaller by about an order of magnitude. Remarkably, evolution of superposed harmonic initial data also shows a speed-up of about 33% compared to superposed Kerr-Schild data for the case considered, reducing the runtime and computational cost of BBH simulations. The speed-up can be traced to the adaptive mesh refinement (AMR) choosing fewer grid points to achieve the same accuracy. We also find that during the initial relaxation, when we intentionally do not attempt to resolve initial transients, the constraint violations converge to zero with increasing resolution only for superposed harmonic initial data.

These positive findings suggest that simulations in the future should use superposed harmonic initial data; however, it is known that a single BH in time-independent horizon-penetrating harmonic coordinates becomes very distorted in the direction of spin for large spins (cf. Fig. 10). These distortions are inherited by the superposed harmonic BBH initial data sets, so that the black hole horizons become so deformed to render evolutions of nearly extremal spins impractical. We find that superposed harmonic initial data works well when both BH dimensionless spin magnitudes are below 0.7.

We also find that superposed damped harmonic initial data does not perform as well as superposed Kerr-Schild initial data in the above respects. However, we find that we can construct superposed Kerr-Schild initial data that is initially in damped harmonic gauge (so as to avoid a subsequent gauge transformation during the evolution), and that this initial data set performs as well as superposed Kerr-Schild with the current quasiequilbrium initial gauge, in the above respects. Therefore, we recommend that superposed harmonic initial data be used for spin magnitudes ≤ 0.7. For higher spins, we recommend superposed Kerr-Schild initial data with damped harmonic initial gauge, since this performs no worse than the current choice of superposed Kerr-Schild with quasi-equilibrium initial gauge, and it is simpler because it requires no gauge transition during evolution.

The rest of the paper is organized as follows. Section II provides a brief overview of the initial data formalism, including the new negative-expansion boundary conditions and new choices of free data and initial gauge. In Sec. III we summarize the particular choices of initial data that we choose to construct and compare in this work. In Sec. IV we test convergence of constraints in

each of these initial data sets. In Sec. V we evolve these different initial data sets and compare the results of these evolutions. Finally, in Sec. VI we provide a conclusion and recommendations for the construction of initial data in future BBH simulations. Throughout this paper we use geometric units with $G = c = 1$. We use Latin letters from the start of the alphabet $(a, b, c, \dots)$ for spacetime indices and from the middle of the alphabet $(i, j, k, \dots)$ for spatial indices. We use ψ_{ab} for the space-time metric. We use g_{ij} for the spatial metric, N for the lapse and N^i for the shift of the constant-t hypersurfaces.

We note that this paper focuses entirely on improvements to the initial data treatment adopted by codes [15, 23] that use the generalized harmonic formulation [20–23] of the evolution equations. NR codes [30–36] that use moving-puncture initial data [37] (since they do not employ BH excision) and/or the BSSNOK formulation [30, 38, 39] of the evolution equations (since the gauge is set directly by setting a lapse and a shift, rather than a gauge souce funcion) would not benefit from these improvements.

II. BBH INITIAL DATA FORMALISM

In this section we provide a brief overview of binary black hole initial data formalism, and we suggest improved boundary conditions and gauge choices. We start by discussing the Extended Conformal Thin Sandwich (XCTS) system of elliptic equations in Sec. II A. Next, in Sec. II B we cover the boundary conditions for the elliptic equations, including the new negative expansion boundary conditions that lets us avoid spatial extrapolation of the initial data quantities. Finally, in Sec. II C we discuss different gauge choices that we use in initial data. In the next section, Sec. III, we summarize the different initial data sets constructed for this study.

A. Extended conformal thin sandwich equations

XCTS [16, 17] is a formulation of the Einstein constraint equations well-suited for numerical solution. The "extended" part of XCTS refers to an additional equation that is added to the system: the evolution equation for the trace of the extrinsic curvature, converted into an elliptic equation. This extra equation is useful in producing initial data in quasi-equilibrium. For a more detailed review of initial data construction, see [40–42].

The XCTS construction starts with a conformal decomposition of the 3-metric into a conformal factor ψ and a conformal metric $\bar{g}_{ij}$

$$g_{ij} = \psi^4 \, \bar{g}_{ij}. \tag{1}$$

Using the definition of extrinsic curvature in terms of the time derivative of the spatial metric, the extrinsic curvature K_{ij} takes the form

$$K_{ij} = \frac{1}{3} g_{ij} K + A_{ij}, \tag{2}$$

where

$$A_{ij} = \psi^{-2} \bar{A}_{ij}, \quad \bar{A}^{ij} = \frac{\psi^6}{2N} \left((\bar{\mathbb{L}} N)^{ij} - \bar{u}^{ij} \right). \tag{3}$$

Here N is the lapse, N^i is the shift, $(\bar{\mathbb{L}} N)^{ij}$ represents the conformal Killing operator in conformal space, and $\bar{u}_{ij} = \partial_t \bar{g}_{ij}$[1]. K and A_{ij} are the trace and trace-free part of K_{ij}.

In the XCTS formalism, one can freely specify the conformal metric $\bar{g}_{ij}$, trace of extrinsic curvature K, and their time derivatives $\bar{u}_{ij}$ and $\partial_t K$. For quasi-equilibrium situations, these time derivatives are typically set to zero. The system of of elliptic equations to be solved becomes:

$$\bar{\nabla}^2 \psi - \frac{1}{8} \bar{R} \psi - \frac{1}{12} K^2 \psi^5 + \frac{1}{8} \psi^{-7} \bar{A}^{ij} \bar{A}_{ij} = 0, \tag{4}$$

$$\bar{\nabla}_j \left(\frac{\psi^6}{2N} (\bar{\mathbb{L}} N)^{ij} \right) - \frac{2}{3} \psi^6 \bar{\nabla}^i K - \bar{\nabla}_j \left(\frac{\psi^6}{2N} \bar{u}^{ij} \right) = 0, \tag{5}$$

$$\bar{\nabla}^2 (N\psi) - N\psi \left(\frac{\bar{R}}{8} + \frac{5}{12} K^4 \psi^4 + \frac{7}{8} \psi^{-8} \bar{A}^{ij} \bar{A}_{ij} \right) + \psi^5 (\partial_t K - N^k \partial_k K) = 0, \tag{6}$$

where $\bar{R}$ and $\bar{\nabla}_i$ are the Ricci scalar and the spatial covariant derivative operator associated with $\bar{g}_{ij}$. Once these equations are solved for ψ, $N\psi$ and N^i, the physical solution (g_{ij}, K_{ij}) is constructed from Eqs. (1-3) and the free data ($\bar{g}_{ij}$, $\bar{u}_{ij}$, K and $\partial_t K$).

1. *Choosing freely specifiable data*

If the lapse N and shift N^i computed from XCTS are used in the evolution of the initial data, the time derivative of K will initially be equal to the specified $\partial_t K$ and the trace-free part of $\partial_t g_{ij}$ will be initially proportional to the specified $\bar{u}_{ij}$. In order to generate quasi-equilibrium initial data, the natural choice for these freely specifiable quantities is:

$$\bar{u}_{ij} = 0, \quad \partial_t K = 0. \tag{7}$$

Following Ref. [18], we construct the free data based on a superposition of two single-BH solutions. Let g^α_{ij} and K^α be the 3-metric and the trace of extrinsic curvature of a single boosted, spinning black hole, with $\alpha = 1, 2$ labeling the two black holes. We then choose the conformal 3-metric $\bar{g}_{ij}$ and the trace of the extrinsic curvature

[1] Note that one also needs to set $\bar{g}^{ij} \bar{u}_{ij} = 0$ to uniquely specify $\bar{u}_{ij}$.

K to be

$$\bar{g}_{ij} = f_{ij} + \sum_{\alpha=1}^{2} e^{-r_\alpha^2/w_\alpha^2}\ (g_{ij}^\alpha - f_{ij}), \tag{8}$$

$$K = \sum_{\alpha=1}^{2} e^{-r_\alpha^2/w_\alpha^2} K^\alpha, \tag{9}$$

where f_{ij} is the flat 3-metric. Far from the holes, the conformal metric is very nearly flat and the trace of extrinsic curvature is very nearly zero. This is achieved through a Gaussian weight around each hole, with a width w_α that determines how fast the conformal metric approaches the flat metric with increasing Euclidean distance r_α from the center of each hole. The widths of the Gaussians w_α are chosen to be

$$w_\alpha = 0.6\ d_\alpha^{L_1}, \tag{10}$$

where $d_\alpha^{L_1}$ is the Euclidean distance to the Newtonian L_1 Lagrange point from the center of hole α. This is identical to the choice made in Ref. [18]. This ensures that the widths are larger than the size scale of the hole ($\sim M_\alpha$, the mass of the hole) but smaller than the distance to the other hole. This also ensures that near each black hole, the contributions of the other black hole are attenuated by several orders of magnitude. The Gaussians are also needed so that at large distances the solution does not develop a logarithmic singularity [43].

The single-BH quantities g_{ij}^α and K^α above are determined by the Kerr metric, by a choice of how to slice the Kerr metric into a foliation of three-dimensional hypersurfaces, and by a choice of spatial coordinates on these hypersurfaces. These choices are largely arbitrary, but they must satisfy certain conditions to produce a viable initial data set; for example, the slices must contain an apparent horizon and be regular there.

2. *Exploring new choices of free data*

A key goal of this paper is to investigate the effect of the choice of g_{ij}^α and K^α on the resulting initial data set and subsequent evolution. Here we consider three choices, explained in more detail in Sec. III. The first is the choice made in the current implementation of SpEC, which was introduced in Ref. [18]: g_{ij}^α and K^α are taken to be in Kerr-Schild coordinates centered about each BH. The second is to specify g_{ij}^α and K^α in harmonic coordinates, using the unique harmonic time slicing that is both time-independent (for a single BH) and that penetrates the horizon as derived in Ref. [28]. Finally, we also consider the case in which g_{ij}^α and K^α are chosen in the unique coordinate system that obeys the damped harmonic condition [25–27] and for which the time slices are time-independent and horizon-penetrating [29]. For all of these cases, we use the same Gaussian weights in Eqs. (8) and (9).

B. Boundary conditions

Equations (4), (5), and (6) require appropriate boundary conditions in order to solve for initial data.

The outer boundary (denoted by $\mathcal{B}_\infty$) conditions are obtained by requiring the initial data to be asymptotically flat. Note that in practice, we do not actually place the boundary $\mathcal{B}_\infty$ at spatial infinity, but at a coordinate sphere of radius $\sim 10^9 M$. Because the conformal metric and trace of extrinsic curvature, as given by Eqs. (8) and (9), are already asymptotically flat, the outer boundary conditions are

$$\psi = 1 \quad \text{at } \mathcal{B}_\infty, \tag{11}$$

$$N\psi = 1 \quad \text{at } \mathcal{B}_\infty, \tag{12}$$

$$\widetilde{N}^i = (\mathbf{\Omega_0} \times \mathbf{r})^i + \dot{a}_0 r^i \quad \text{at } \mathcal{B}_\infty. \tag{13}$$

Here, $\widetilde{N}^i$ is the shift in a frame that co-rotates with the binary, r^i is the coordinate position vector, $\mathbf{\Omega_0}$ is the orbital angular velocity and $\dot{a}_0$ is an expansion parameter. The shift boundary condition consists of a rotation and an expansion term. The rotation term (parametrized by $\mathbf{\Omega_0}$) ensures that the time coordinate is helical and tracks the rotation of the system, and the expansion term (parametrized by $\dot{a}$) sets a non-zero radial velocity, to account for the initial decrease in the orbit due to radiation reaction. These boundary conditions are identical to those in [44], which presents a more detailed exposition.

The inner boundary conditions are imposed on the excision surfaces, denoted by $\mathcal{B}_E$. These are chosen to be surfaces of constant radial coordinate in the single BH coordinates used in Eq. 8. We choose our single BH coordinates such that the apparent horizon has a constant radial coordinate[2] but the excision boundary may or may not be an apparent horizon, as explained below. Here we consider two types of inner boundary conditions.

1. *Horizon boundary conditions*

The standard practice in SpEC has been to choose quasi-equilibrium apparent/isolated horizon boundary conditions on the inner excision surfaces[19, 45]. We refer the reader to [40, 46, 47] for a review of the properties of apparent and isolated horizons. We require boundary conditions on the conformal factor, the shift vector, and the lapse function.

The boundary condition for the conformal factor is obtained by setting the expansion scalar on the excision surface to zero, ensuring that it is an apparent horizon. To see how this results in a boundary condition, we first

[2] For superposed Kerr-Schild and superposed harmonic, this is the Boyer-Lindquist radius; for superposed damped harmonic, this coordinate is determined numerically [29].

write out the expansion of $\mathcal{B}_E$ as

$$\Theta = \frac{4}{\psi^3}\left[\bar{s}^k\,\partial_k\psi + \frac{\psi^3}{8N}\bar{s}^i\bar{s}^j\left((\bar{\mathbb{L}}N)_{ij} - \bar{u}_{ij}\right) + \frac{\psi}{4}\bar{h}^{ij}\bar{\nabla}_i\bar{s}_j - \frac{1}{6}K\psi^3\right], \tag{14}$$

where $\bar{s}^i = \psi^2 s^i$, s^i is the spatial unit normal to $\mathcal{B}_E$, and $\bar{h}_{ij} = \bar{g}_{ij} - \bar{s}_i\bar{s}_j$ is the induced conformal 2-metric on $\mathcal{B}_E$. $\bar{h}_{ij}$ is related to the induced 2-metric on $\mathcal{B}_E$ by $h_{ij} = \psi^4\bar{h}_{ij}$. Enforcing the excision surfaces to be apparent horizons (setting $\Theta = 0$) gives us a boundary condition on the conformal factor at $\mathcal{B}_E$:

$$\bar{s}^k\,\partial_k\psi = -\frac{\psi^3}{8N}\bar{s}^i\bar{s}^j\left((\bar{\mathbb{L}}N)_{ij} - \bar{u}_{ij}\right) - \frac{\psi}{4}\bar{h}^{ij}\bar{\nabla}_i\bar{s}_j + \frac{1}{6}K\psi^3. \tag{15}$$

The boundary condition on the shift is obtained by requiring that: (1) The coordinate location of the apparent horizons do not change (in a co-rotating frame) as the initial data begin to evolve. (2) The shear tensor vanishes on the excision surface; this is a property of isolated horizons [46]. We impose these two conditions only approximately, as described below. To obtain the shift boundary condition, we first decompose the shift into parts normal and tangential to the surface $\mathcal{B}_E$,

$$N^i = N^i_{\parallel} + N_{\perp}s^i, \tag{16}$$

where

$$N^i_{\parallel} \equiv h^i_j N^j, \tag{17}$$

$$N_{\perp} \equiv N^i s_i. \tag{18}$$

The inner boundary condition (at $\mathcal{B}_E$) for the shift is

$$N_{\perp} = N, \tag{19}$$

$$N^i_{\parallel} = -\Omega^{(k)}_r\xi^i_{(k)}, \tag{20}$$

where

$$\vec{\xi}_{(0)} = y\hat{z} - z\hat{y}, \tag{21}$$

$$\vec{\xi}_{(1)} = z\hat{x} - x\hat{z}, \tag{22}$$

$$\vec{\xi}_{(2)} = x\hat{y} - y\hat{x} \tag{23}$$

are three linearly independent conformal Killing vectors of a coordinate sphere, and $\Omega^{(k)}_r$ are three arbitrarily specifiable free parameters that will be discussed below. The first condition, Eq. (19), ensures the apparent horizons are initially at rest in the coordinates. The second condition, Eq. (20), sets the spin of the black hole [19, 45]. If the excision surface is a coordinate sphere, then $\vec{\xi}_{(k)}$ are conformal Killing vectors associated with $\bar{h}_{ij}$, $\vec{\xi}_{(k)}$ are orthogonal to s_i, and the shear tensor vanishes on the excision surface [19]. For the initial data choices compared here, the excision boundary is not a coordinate sphere, so neither the shear-free condition nor the stationary-horizon condition that motivated the shift boundary conditions are satisfied. Nevertheless, we find that the boundary conditions above are adequate for binary black hole initial data.

In practice, it is not possible to *a priori* choose values of $\Omega^{(k)}_r$ that will yield a desired black hole spin; instead one must use an iterative procedure [48, 49], where at each iteration $\Omega^{(k)}_r$ is updated until the spin converges to the desired value. For each iteration, the spin parameter in the single-black-hole solutions $\bar{g}^{\alpha}_{ij}$ and K^{α} (cf. Eqs. (8) and (9)) is unchanged, and is set to the desired black hole spin.

Finally, the boundary condition at $\mathcal{B}_E$ for the lapse (which can be chosen freely [19]) is chosen such that its value in the vicinity of each black hole approaches that of the corresponding single black hole lapse,

$$N\psi = 1 + \sum_{\alpha=1}^{2} e^{-r_\alpha^2/w_\alpha^2}(N_\alpha - 1), \tag{24}$$

where N_α is the lapse corresponding to single black hole α and the Gaussian weights are the same as in Eq. (8).

2. *Negative expansion boundary conditions*

The horizon boundary conditions discussed above enforce the excision surfaces to be apparent horizons. However, BBH evolutions require an inner boundary that is slightly *inside* the apparent horizons, for the following reasons: (1) The apparent horizons dynamically change shape and size during evolution, so if the excision surfaces are *at* the apparent horizons, the horizons can fall off the numerical grid during evolution. (2) Our method of finding apparent horizons during the evolution needs to explore regions just inside and just outside of the horizon in order to converge onto the correct surface. (3) During the evolution, no boundary conditions need to be imposed at the inner boundary, because all characteristic fields are ingoing (into the black hole) there. To maintain this ingoing-characteristic-fields condition, the inner boundary is adjusted to closely track the apparent horizon to within a small but nonzero error tolerance.

This means that after solving for initial data using horizon boundary conditions, the initial data must be extrapolated spatially to a new grid that has smaller excision surfaces. This extrapolation introduces constraint violations (cf. left panel of Fig. 1), and therefore we propose new boundary conditions that are similar to the horizon boundary conditions discussed above but are set on a surface inside the horizon and thus avoid extrapolation altogether.

The idea behind the new boundary conditions is to set the expansion not to zero, but to some nonzero value that ensures that the excision boundary is inside an apparent horizon rather than on one. We use Eq. (14) to modify

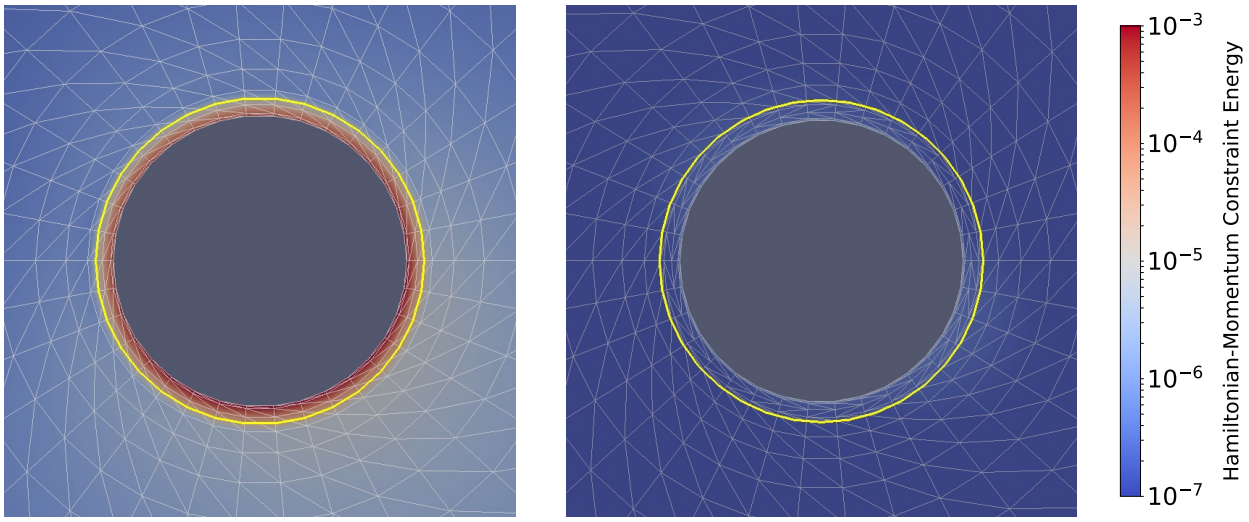

FIG. 1. Initial constraint violations on the $z = 0$ plane near the larger hole of a BBH system, for horizon boundary conditions (left) and negative expansion boundary conditions (right). Colors show the magnitude of the Hamiltonian-momentum constraint energy (cf. Eq. 42), the yellow circle is the apparent horizon, and the large black area inside the horizon is the excision region. Here superposed Kerr-Schild free data are used to construct a BBH with mass ratio $q = 1.1$ and spins $\chi_{1z} = -0.3$ and $\chi_{2z} = -0.4$ along the direction of orbital angular momentum. Unlike the horizon boundary conditions, the negative expansion boundary conditions require no extrapolation inside the horizon, and thus yield constraints near and inside the apparent horizon that are about 3 orders of magnitude smaller.

the conformal factor boundary condition at $\mathcal{B}_E$ to:

$$\bar{s}^k\ \partial_k\psi = -\frac{\psi^3}{8N}\bar{s}^i\bar{s}^j\left((\bar{\mathbb{L}}N)_{ij} - \bar{u}_{ij}\right) - \frac{\psi}{4}\bar{h}^{ij}\bar{\nabla}_i\bar{s}_j + \frac{1}{6}K\psi^3 + \frac{\psi^3}{4}\Theta_\alpha, \qquad (25)$$

where α denotes the particular BH and Θ_α is computed from the single BH metrics used in Eq. 8. As we choose the excision surface to be slightly inside the single BH horizons, Θ_α is negative on the surface. Henceforth we refer to this boundary condition as a negative expansion boundary condition.

When imposing the negative expansion condition, we also need to modify the shift boundary condition, as Eq. (19) holds only on a horizon. Noting that for a single BH, $\epsilon = N_\perp - N$ is positive inside the horizon and negative outside, we modify the boundary condition at $\mathcal{B}_E$ for the normal component of shift to:

$$N_\perp = N + \epsilon_\alpha, \qquad (26)$$

where $\epsilon_\alpha = N_{\perp\alpha} - N_\alpha$ are again obtained from the single BH solutions of the individual holes.

For negative expansion boundary conditions, we continue to use Eq. (20) for the tangential part of the shift. We also continue to use Eq. (24) for the boundary condition on the lapse, with N_α evaluated at the new location of the inner boundary. We find that the procedure for setting the spin via iteration over $\Omega_r^{(k)}$, as described in Sec. II B 1, works just as well in the case of a negative expansion BC as it does for a horizon BC.

Figure 1 demonstrates the efficacy of these new boundary conditions; shown are the constraints near the larger black hole when using horizon boundary conditions and the new negative expansion boundary conditions. When using negative expansion boundary conditions, the constraints improve by about 3 orders of magnitude inside and near the apparent horizon. Note, however, that once the evolution begins, most of this constraint violation propagates inwards into the excision surfaces and out of the computational domain. This is because in the generalized harmonic formalism the evolution of constraint violations is governed by a wave equation [20], which ensures that constraint violations propagate causally. Hence, we do not expect the new boundary conditions to reduce constraint violations during the evolution nearly as much as they improve initial constraint violations.

C. Gauge choices

SpEC uses the generalized harmonic evolution system [20–23] to evolve the initial data. In this formalism, the gauge choice is set by requiring the coordinates to satisfy an inhomogeneous wave equation,

$$-{}^{(4)}\Gamma^a = \nabla^c\nabla_c x^a = H^a, \qquad (27)$$

where ${}^{(4)}\Gamma^a = \psi^{bc}\,{}^{(4)}\Gamma^a_{bc}$, ψ_{ab} is the spacetime metric, ${}^{(4)}\Gamma^a_{bc}$ are the Christoffel symbols associated with ψ_{ab}, ∇_a is the covariant derivative operator compatible with ψ_{ab}, and H^a (called the gauge source function) is a function

of the coordinates x^a and the metric ψ_{ab} (but not the derivatives of the metric).

The simplest choice for the gauge source function is to set it to zero, which yields the harmonic gauge:

$$\nabla^c \nabla_c x^a = H^a = 0. \tag{28}$$

Harmonic coordinates have proven to be extremely useful in analytic studies in GR [28, 50–53]. However, this gauge does not work well for simulations of black hole mergers. One common reason for the failure is growth in $\sqrt{g}/N$, which tends to blow up as the black holes approach each other [27].

SpEC evolutions are done instead in the damped harmonic gauge [27] given by:

$$\nabla^c \nabla_c x^a = H^a_{DH}, \tag{29}$$

$$H^a_{DH} \equiv \mu_L \log\left(\frac{\sqrt{g}}{N}\right) t^a - \mu_S \frac{N^i}{N} g^a{}_i, \tag{30}$$

where t^a is the future directed unit normal to constant-t hypersurfaces, g_{ab} is the spatial metric of the constant-t hypersurfaces and g its determinant, and μ_L and μ_S are positive damping factors that can be chosen arbitrarily. The spatial coordinates and lapse satisfy a damped wave equation with damping factors μ_S and μ_L, and are driven towards solutions of the covariant spatial Laplace equation on timescales of $1/\mu_S$ and $1/\mu_L$, respectively. Damped harmonic gauge tends to reduce extraneous gauge dynamics present in the harmonic gauge.

The damping factors are chosen as follows:

$$\mu_S = \mu_L = \mu_0 \left[\log\left(\frac{\sqrt{g}}{N}\right)\right]^2, \tag{31}$$

where $M\mu_0$ is chosen to be of order unity, and μ_0 is a function of time (to accommodate starting an evolution from initial data satisfying a different gauge condition). This choice of the damping factors ensures that $\sqrt{g}/N$ is driven faster than exponentially towards an asymptotic state [27], so that $\sqrt{g}/N$ does not grow rapidly near mergers as often happens with harmonic gauge.

1. *Setting the initial gauge*

The generalized harmonic evolution system requires the metric ψ_{ab} and its time derivative $\partial_t \psi_{ab}$ to be specified on the initial time slice. Most of these quantities are determined by the solution of the XCTS equations and the free data that are used in solving these equations. However, $\partial_t \psi_{ab}$ also includes the time derivatives of the lapse and shift, which are independent of the XCTS equations. Instead, they are equivalent to the initial choice of the gauge source function H^a. To see this, we expand the generalized harmonic gauge condition, Eq. (27), and rewrite it in terms of the time derivatives of lapse and shift:

$$\partial_t N = N^j \partial_j N - N^2 K + N^3 H^0, \tag{32}$$

$$\partial_t N^i = N^j \partial_j N^i - N^2 g^{ij} \partial_j (\log N) + N^2 \Gamma^i + N^2 (H^i + N^i H^0). \tag{33}$$

Here $\Gamma^i = g^{jk}\Gamma^i_{jk}$ and Γ^i_{jk} are the Christoffel symbols associated with g_{ij}. Note that N^2 and N^3 indicates powers of the lapse function, whereas N^i, H^0 and H^i are components of the shift-vector N^i and the gauge-source function H^a.

The default choice in SpEC simulations has been to set $\partial_t N = \partial_t N^i = 0$ in a frame co-rotating with the binary; this is meant to be a quasiequilibrium condition that reduces initial gauge dynamics. Given this choice, Eqs. (32) and (33) determine the initial values of H^a, which are kept time-independent in this co-rotating frame during the initial stages of the evolution. However, the damped harmonic gauge works best for mergers, so SpEC simulations customarily move from co-rotating gauge to damped harmonic gauge via a smooth gauge transformation during the first $\sim 50M$ of the evolution. However, this gauge transformation introduces additional complications: (1) The gauge change causes additional gauge dynamics in the evolution. (2) The gauge change happens at the same time as the junk radiation leaves the system, making it difficult to distinguish junk radiation from gauge dynamics. (3) The gauge change impacts the ability to achieve configurations with zero orbital eccentricity. To understand this last point, we note that SpEC evolutions customarily employ iterative eccentricity reduction [54]: Starting with orbital parameters predicted by post-Newtonian theory, we evolve the binary for ~ 2 orbits, compute the eccentricity, adjust the initial parameters and repeat until the desired eccentricity is achieved. This involves an extrapolation back in time to compute adjusted parameters and this extrapolation happens at the same time as the gauge transformation.

2. *New choices of initial gauge*

With the aim of addressing these issues, as part of this work we have also explored setting the initial gauge to satisfy the harmonic or damped harmonic condition, as explained in more detail in Sec. III. In order to set the initial gauge to the harmonic or damped harmonic gauge, we set $\partial_t N$ and $\partial_t N^i$ according to Eqs. (32) and (33) at $t = 0$, with $H^a = 0$ for harmonic gauge and $H^a = H^a_{DH}$ for damped harmonic gauge.

III. BBH INITIAL DATA TYPES

Having introduced the BBH initial data formalism, in this section we discuss the different initial data sets con-

Type	Initial Data		Evolution	
	XCTS free data ($\bar{g}_{ij}$, K)	Inner BC	Initial Gauge	Final Gauge
SKS-Eq-θ_0	Superposed Kerr-Schild	Horizon BC	Quasi-equilibrium	Damped Harmonic
SKS-Eq	Superposed Kerr-Schild	Negative expansion BC	Quasi-equilibrium	Damped Harmonic
SH-H	Superposed Harmonic	Negative expansion BC	Harmonic	Damped Harmonic
SDH-DH	Superposed Damped Harmonic	Negative expansion BC	Damped Harmonic	Damped Harmonic
SKS-DH	Superposed Kerr-Schild	Negative expansion BC	Damped Harmonic	Damped Harmonic

TABLE I. Types of initial data considered in this study. The initial data formalism is described in Sec. II. See Sec. II A for the XCTS system of equations and Sec. II A 1 for the freely specifiable data in XCTS. We describe the horizon boundary conditions in Sec. II B 1 and negative expansion boundary conditions in Sec. II B 2. The gauge choices are described in Sec. II C. The initial gauge is chosen by setting $\partial_t N$ and $\partial_t N^i$ according to Sec. II C 1.

sidered in this study; these are also listed in Table I. Our naming convention for the initial data sets indicates the choice of free data, initial gauge condition and boundary conditions at excision surfaces. For example, SKS-Eq-θ_0 stands for superposed Kerr-Schild free data, quasi-equilibrium initial gauge condition, and horizon boundary conditions at excision surfaces. Unless explicitly specified, we use the new negative expansion boundary conditions at excision surfaces.

A. Superposed Kerr-Schild with horizon boundary conditions (SKS-Eq-θ_0)

This is the type of initial data currently implemented in SpEC [18]. Initial data are constructed by solving the XCTS system of equations, with horizon boundary conditions imposed on the excision surfaces. The free data for XCTS equations are obtained using a superposition of two single BHs in the Kerr-Schild gauge. Once the XCTS equations are solved, the initial data are extrapolated slightly inside the apparent horizon surfaces. The initial gauge is set by imposing $\partial_t N = \partial_t N^i = 0$ in a co-rotating frame. During the initial stages of the evolution a smooth gauge transformation moves into the damped harmonic gauge over a time scale of $50M$. We refer to this initial data set as SKS-Eq-θ_0.

B. Superposed Kerr-Schild with negative expansion boundary conditions (SKS-Eq)

This is the same as SKS-Eq-θ_0 above but with a negative expansion boundary condition (Sec. II B 2) on the excision surfaces. We choose the excision surfaces to be slightly inside the apparent horizons and thus avoid the need for extrapolation in initial data. We refer to this as SKS-Eq.

C. Superposed Harmonic-Kerr (SH-H)

The free data are obtained by superposing two single BHs in the harmonic coordinates of Ref. [28]. The time derivatives $\partial_t N$ and $\partial_t N^i$ at $t = 0$ are set according to the Harmonic gauge condition (cf. Eqs. 28, 32 and 33):

$$\partial_t N = N^j \partial_j N - N^2 K, \tag{34}$$

$$\partial_t N^i = N^j \partial_j N^i - N^2 g^{ij} \partial_j (\log N) + N^2 \Gamma^i. \tag{35}$$

Therefore, the initial data is in the harmonic gauge at $t = 0$. As in the case of SKS-Eq, during the initial stages of the evolution we do a smooth gauge transformation to the damped harmonic gauge over a time scale of $50M$. A negative expansion boundary condition (Sec. II B 2) is used on the excision surfaces. We refer to this initial data as SH-H. We find that SH-H initial data works well for dimensionless spin magnitudes $\chi \leq 0.7$; for higher spins the single BHs in harmonic coordinates are highly compressed in the direction of spin (see Fig. 10).

D. Superposed Damped Harmonic (SDH-DH)

The free data are obtained by superposing two single BHs in the damped harmonic gauge of Ref. [29], and a negative expansion boundary condition (Sec. II B 2) is used on the excision surfaces. $\partial_t N$ and $\partial_t N^i$ at $t = 0$ are set according to the damped harmonic gauge condition, Eqs. (30), (32) and (33):

$$\partial_t N = N^j \partial_j N - N^2 K + N^3 H^0_{DH}, \tag{36}$$

$$\partial_t N^i = N^j \partial_j N^i - N^2 g^{ij} \partial_j (\log N) + N^2 \Gamma^i + N^2 (H^i_{DH} + N^i H^0_{DH}). \tag{37}$$

Because the initial data are already in the damped harmonic gauge at $t = 0$, no gauge transformation is necessary during the evolution. We refer to this initial data set as SDH-DH.

E. Superposed Kerr-Schild with Damped Harmonic Gauge (SKS-DH)

This is the same as SKS-Eq, except the initial gauge is set to the damped harmonic gauge using Eqs. (36) and (37). Because the damped harmonic gauge condition is satisfied at $t = 0$, no gauge transformation is needed

during evolution. We refer to these initial data as SKS-DH. Although the motivation for SKS-DH is to avoid the smooth gauge transformation during the evolution, for SKS-DH the gauge is not in quasi-equilibrium at $t = 0$ even if the BHs are far apart; this could potentially lead to more gauge dynamics at the start of the evolution.

IV. CONVERGENCE OF INITIAL DATA

In this section, we perform a convergence test of the different initial data sets we construct. We use the spectral elliptic solver described in Refs. [48, 55] to solve the XCTS equations. We compare the Hamiltonian and momentum constraint violations at different resolutions, for the case of a nonprecessing BBH system with mass ratio $q = 1.1$ and dimensionless spins $\chi_{1z} = -0.3$, $\chi_{2z} = -0.4$ along the orbital angular momentum direction. The Hamiltonian and momentum constraints in vacuum are given by:

$$R + K^2 - K_{ij}K^{ij} = 0, \tag{38}$$

$$g^{jk}(\nabla_j K_{ki} - \nabla_i K_{jk}) = 0, \tag{39}$$

where R and ∇_i are the Ricci scalar and the spatial covariant derivative operator associated with g_{ij}. We quantify these constraint violations by computing their L^2 norms over the initial data domain. We also normalize them to obtain dimensionless quantities [3],

$$\mathcal{H} = \frac{\|R + K^2 - K_{ij}K^{ij}\|}{\left\|\sqrt{\sum_{i,j,k}[(R_{ij}g^{ij})^2 + (K_{ij}K_{kl}g^{ik}g^{jl})^2 + (K_{ij}K_{kl}g^{ij}g^{kl})^2]}\right\|}, \tag{40}$$

$$\mathcal{M}_i = \frac{\|g^{jk}(\nabla_j K_{ki} - \nabla_i K_{jk})\|}{\left\|\sqrt{\sum_{i,j,k}\left[(g^{jk})^2((\nabla_j K_{ki})^2 + (\nabla_i K_{jk})^2)\right]}\right\|}, \tag{41}$$

where $\|.\|$ denotes the L^2 norm over the domain. Finally, we define a Hamiltonian-Momentum constraint energy:

$$\mathcal{C} = \sqrt{\mathcal{H}^2 + \sum_{i=0}^{2} \mathcal{M}_i^2}\,. \tag{42}$$

Figure 2 shows a convergence test for the different initial data sets considered in this study. We see exponential convergence in all cases, as is expected with spectral methods. For SKS-Eq-θ_0, while we see exponential convergence for the constraints before extrapolation, the constraints after extrapolation are significantly higher.

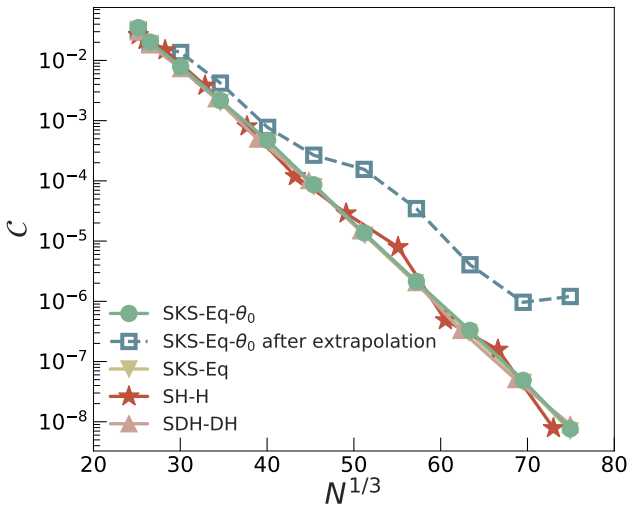

FIG. 2. Convergence test for the spectral elliptic solver in solving the XCTS equations for the different initial data types listed in Table. I. Shown is the Hamiltonian-momentum constraint energy (Eq. 42) vs. the number of collocation points per dimension in the domain. As expected for spectral methods, the constraints decrease exponentially. Also shown are the constraints for SKS-Eq-θ_0 after extrapolation of initial data, where, at high resolution, the constraint violation from extrapolation dominates (cf. Fig. 1). There is no extrapolation for SKS-Eq, SH-H, and SDH-DH, as we use negative expansion boundary conditions for these. Note that SKS-DH is not shown here because its solution of the XCTS equations is identical to SKS-Eq; the cases SKS-Eq and SKS-DH differ only in the initial gauge condition.

This is why we introduced the new negative expansion boundary condition, which avoids extrapolation by placing the excision surface inside rather than at the apparent horizons.

V. BBH EVOLUTION WITH DIFFERENT INITIAL DATA SETS

In this section we evolve the different initial data sets discussed above and compare them for a nonprecessing BBH system with mass ratio $q = 1.1$ and dimensionless spins $\chi_{1z} = -0.3$, $\chi_{2z} = -0.4$ along the orbital angular momentum direction. In particular we look at the constraint violations, gauge evolution, component parameters, extracted waveforms, junk radiation, simulation expense, and ease of constructing zero-eccentricity initial data.

We performed each of these simulations for 5 different resolutions in order to do a convergence study. Each resolution is determined by specifying an error tolerance to our adaptive mesh refinement (AMR) algorithm [56]. In order to match this error tolerance as the evolution proceeds, AMR adds or removes collocation points from each

[3] Notice that for the denominator of Eqs. (40) and (41) as well as Eq. (44) below, repeated indices are summed over *after* squaring the quantities, unlike the standard summation notation.

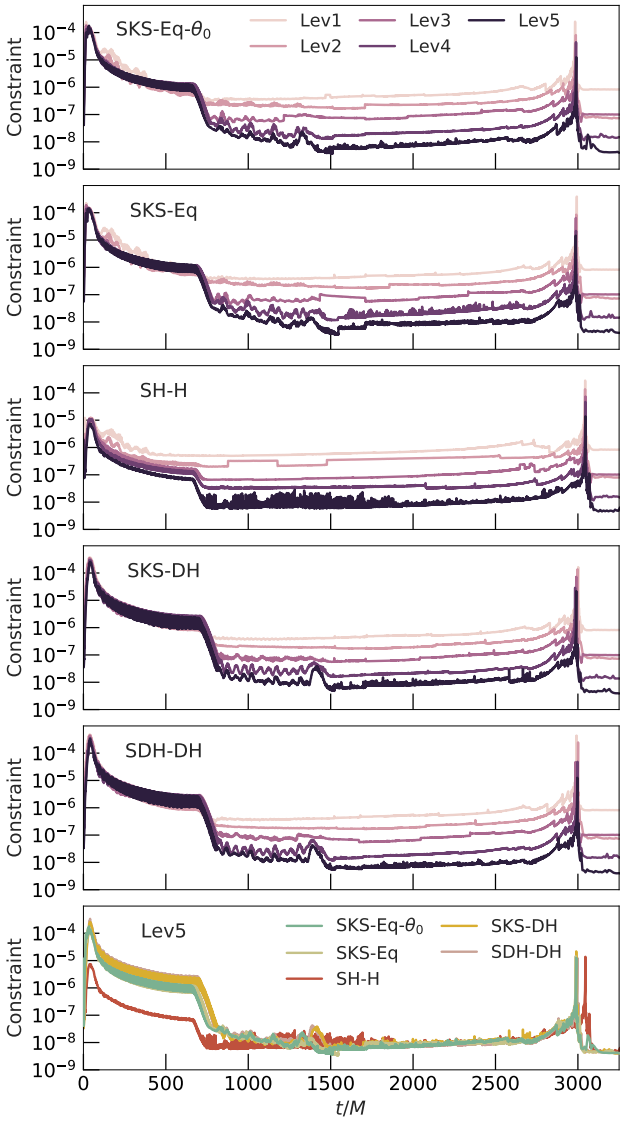

FIG. 3. Convergence test for constraints during evolution using different initial data sets. The top panels show the constraints for different resolutions for each case: Lev1 corresponds to the lowest resolution and Lev5 corresponds to the highest resolution. After the junk radiation leaves the system, we see convergence in all cases. However, we get good convergence during junk radiation stages only for SH-H. The bottom panel shows the constraints for the highest resolution for each case. We see that for SH-H, the constraints during junk radiation are smaller by about an order of magnitude.

subdomain (p-type refinement) and also splits a single subdomain into two or joins two neighboring subdomains as needed (h-type refinement). We use the labels "Lev1" through "Lev5" to indicate decreasing values of AMR error tolerance. During the junk radiation stage, we intentionally prevent the AMR algorithm [56] from resolving the high-frequency features present in the initial transients. This is done because attempting to resolve these features slows down the evolution considerably, and for most purposes (such as comparing with LIGO data) the junk-containing part of the waveforms is removed anyway.

A. Constraint violations

Figure 3 shows the generalized harmonic constraint energy (defined in Eq.(53) of Ref. [20]) during the evolution of the initial data sets for different resolutions. As expected, we see convergence for all the cases after the junk radiation has left the system. Because we intentionally prevent the AMR algorithm from resolving the high-frequency junk-radiation features, it is no surprise that we lose exponential convergence during the junk stage ($t \lesssim 700M$) for most of the cases considered. However, for SH-H initial data, we still retain exponential convergence for most of the junk stage, i.e. for $100M \lesssim t \lesssim 700M$, although with a shallower slope than at later times. This indicates that that there are less prominent high-frequency features present during the junk for SH-H initial data. The bottom panel of Fig. 3 shows the constraints for the highest resolution for different initial data sets. We see that during the initial junk radiation stage, the constraints are lower for SH-H by about an order of magnitude compared to SKS-Eq-θ_0. SDH-DH and SKS-DH initial data sets result in slightly higher constraint violations during junk radiation than SKS-Eq-θ_0, but not by much.

B. Approach to damped harmonic gauge

The evolution of each initial data set discussed above eventually settles into damped harmonic gauge (Eq. 27). For SDH-DH and SKS-DH, the initial data should already be in damped harmonic gauge, and for the other cases damped harmonic gauge is achieved via an explicit gauge transformation. Here we quantify to what extent the evolutions of these initial data sets actually satisfy the damped harmonic gauge condition. Using Eqs. (27) and (29), we define a normalized damped harmonic constraint energy,

$$\mathcal{C}_{DH} = \sqrt{\sum_{a=0}^{3} \mathcal{C}^a_{DH} \mathcal{C}^a_{DH}}\,, \tag{43}$$

$$\mathcal{C}^a_{DH} = \frac{\|{}^{(4)}\Gamma^a + H^a_{DH}\|}{\left\| \sqrt{\sum_{a,b,c=0}^{3} \left[(\psi^{bc}\, {}^{(4)}\Gamma^a_{bc})^2 + (H^a_{DH})^2 \right]} \right\|}, \tag{44}$$

where $\|.\|$ denotes the L^2 norm over the domain. We call this quantity an "energy" because it represents one piece of the constraint energy defined in Eq. (53) of Ref. [20].

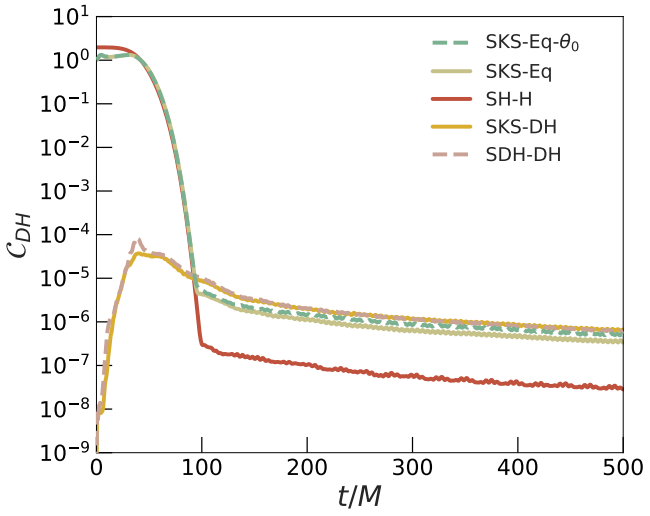

FIG. 4. Damped harmonic constraint energy (Eq. 43) during evolution of different initial data sets. The damped harmonic constraint energy quantifies to what extent the gauge satisfies the damped harmonic condition. For SDH-DH and SKS-DH initial data sets, the initial data are already in the damped harmonic gauge. For the other cases, a smooth gauge transformation is done during early evolution, on a time scale of about $50M$, to move into the damped harmonic gauge. The curves for SKS-Eq-θ_0 and SKS-Eq lie nearly on top of each other.

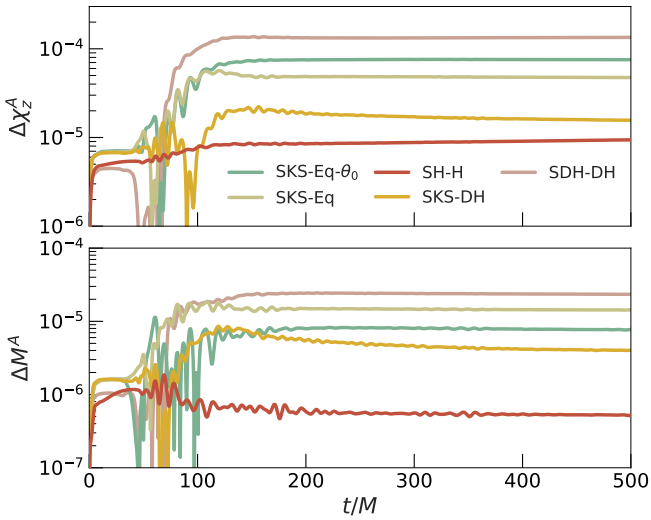

FIG. 5. Behavior of dimensionless spin along the angular momentum direction (top panel) and mass (bottom panel) of the larger black hole during the initial stages of the evolution. Here, $\Delta M^A = |M^A(t) - M^A(t=0)|$ and $\Delta\chi_z^A = |\chi_z^A(t) - \chi_z^A(t=0)|$. The mass and spin are much more stable for SH-H than for the other cases. We attribute this to the small amount of junk radiation in this case; see Sec. V D below.

Figure 4 shows the damped harmonic constraint energy during evolution of different initial data sets. For SDH-DH and SKS-DH, since initial data are already in the damped harmonic gauge, $\mathcal{C}_{DH}$ starts at about 10^{-8}, and rises during the junk radiation stage. However, $\mathcal{C}_{DH}$ always stays below about 10^{-4}. Furthermore, the two methods to generate damped harmonic initial data give rise to comparable $\mathcal{C}_{DH}$. We find that this peak value of 10^{-4} does not change significantly with resolution. This is understandable, as this is caused by junk radiation, which we intentionally do not fully resolve. SKS-Eq-θ_0, SKS-Eq, and SH-H start in a different gauge, and there is no reason to expect small $\mathcal{C}_{DH}$ at $t = 0$. $\mathcal{C}_{DH}$ falls as the evolution transitions to damped harmonic gauge around $t \sim 50M$. The damped harmonic constraint values after the gauge transformation are lower for SH-H than for all the other cases because of smaller junk radiation content, as we will see in Sec. V D below.

C. Component parameters

At the start of the evolution, the component spins and masses change slightly with time. This typically results in slightly lower spins than what we start with. These changes occur as a result of initial transients such as junk radiation leaving the system. Note also that in our initial data we do not tidally deform the BHs. Hence, the initial component parameters can change as the BHs settle down into their equilibrium shapes. Figure 5 shows the change in mass and spin of the larger black hole (with respect to the simulation input parameters), as the simulation progress. We see that the component parameters are more stable by about an order of magnitude for the SH-H initial data compared to SKS-Eq-θ_0. SDH-DH initial data results in the largest changes while SKS-DH does better than SKS-Eq-θ_0. In Sec. V D we will see that this can be attributed to the amount of junk radiation for each of these initial data sets. Note that Fig. 5 corresponds to the highest resolution (Lev=5) used for this study. Repeating Fig. 5 with a lower resolution results in changes on the order of 10^{-4} in spin and 10^{-5} in mass for all cases except SH-H, and changes on the order of 10^{-5} in spin and 10^{-6} in mass for SH-H. Since the changes with resolution are on the same order as the variations shown in the figure, the curves in Fig. 5 should be regarded only as order of magnitude estimates. For all resolutions, the variations in mass and spin for SH-H are smaller than for the other cases.

D. Waveform comparison

Figure 6 shows the gravitational waveforms obtained by the evolution of the different initial data sets. The waveforms are extracted at different extraction radii up to $600M$ from the origin and extrapolated to spatial infinity [57]. The left column shows different spin weighted

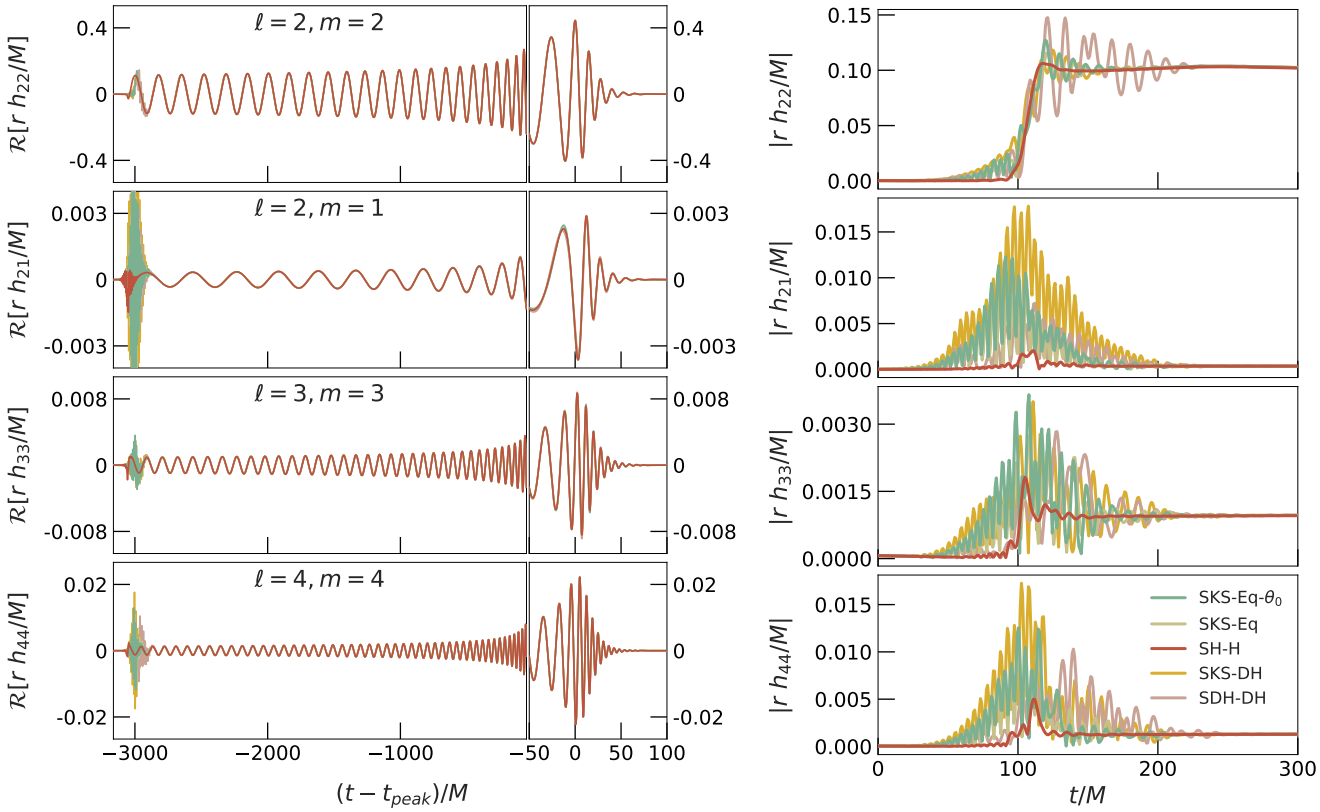

FIG. 6. Comparison of the waveforms resulting from evolution of different initial data sets. The left column shows the real parts of different spin-weighted spherical harmonic modes. The waveforms are aligned by time-shifting them so that the peak amplitude occurs at $t = 0$, and phase-shifting them so that the orbital phase is zero at $t = 0$. Once the junk radiation leaves the domain, the waveforms agree very well between the different initial data sets. The right panels show the amplitudes of the different modes (without any time-shifting) during the junk radiation stage. We see that SH-H initial data results in the least amount of junk radiation. SDH-DH initial data, on the other hand, leads to the most junk radiation. Note however, that junk radiation is not well resolved for all cases except SH-H (cf. Fig 3), hence the amount of junk radiation changes significantly with resolution.

spherical harmonic modes of the waveform (we only show the real parts of the modes here; the imaginary parts have very similar features). As expected, after the initial junk radiation stage the waveforms between the different initial data sets agree very well.

The right panels of Fig. 6 show the amplitudes of different modes during the junk radiation stage. Among all the initial data sets considered here, the junk radiation is the least in the case of SH-H initial data. Compared to the current implementation in SpEC (SKS-Eq-θ_0), the junk radiation decreases by a significant amount for SH-H initial data. The junk radiation also leaves the system much faster in this case.

As noted before, when evolving most initial data sets we perform a smooth time-dependent gauge transformation so that the system settles into damped harmonic gauge on a time scale of $50M$ after the start of the evolution. The SDH-DH and SKS-DH initial data sets already satisfy the damped harmonic condition at $t = 0$, so there is no need for such a gauge transformation. We see that, among the cases considered, the junk radiation is largest in the case of SDH-DH initial data. For SKS-DH initial data, the junk radiation is at a comparable level to SKS-Eq-θ_0. This suggests that we lose nothing by choosing the simpler SKS-DH initial data over the standard choice of SKS-Eq-θ_0. We also confirm that, as expected, the amount of junk radiation is roughly independent of initial gauge, but depends on the free data.

We can quantify the agreement between any pair of waveforms by the mismatch[4] between them:

$$\mathcal{MM} = 1 - \frac{\langle h_1, h_2\rangle}{\sqrt{\langle h_1, h_1\rangle \langle h_2, h_2\rangle}}, \tag{45}$$

$$\langle h_1, h_2\rangle = 4\mathcal{R}\left[\int_{f_{min}}^{f_{max}} \tilde{h}_1(f)\tilde{h}_2^*(f)\, df\right], \tag{46}$$

[4] We choose to use a flat noise curve so that our statements are independent of the choice of GW detector.

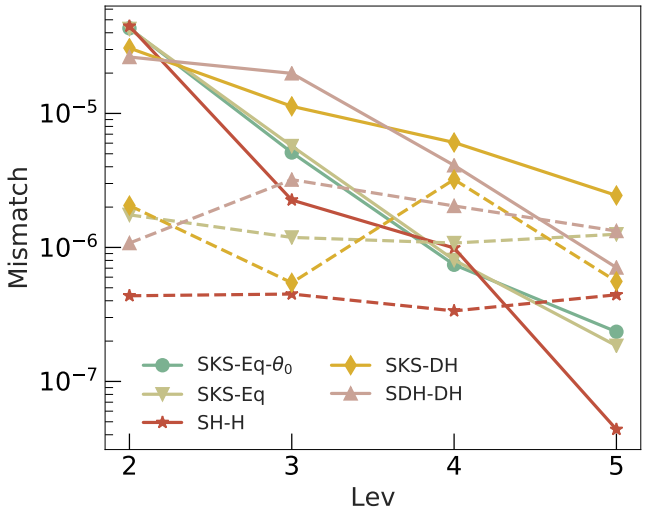

FIG. 7. Median mismatches across the sky in the source frame between waveforms generated from different initial data sets, as a function of numerical resolution. The horizontal axis shows the numerical resolution; we ran at five different numerical resolutions labeled from lowest (Lev=1) to highest (Lev=5). The solid lines represent numerical resolution error: they compare the waveform at the labeled Lev to that of Lev−1. Dashed lines show the differences between the waveform generated from evolving the labeled initial data set to that generated from evolving SKS-Eq-θ_0. The numerical resolution errors show reasonable convergence, as expected. Interestingly, the mismatch between different initial data sets does not change significantly with resolution. For sufficiently high resolution, the resolution errors become smaller than initial data differences. See discussion in Sec. V D for more details.

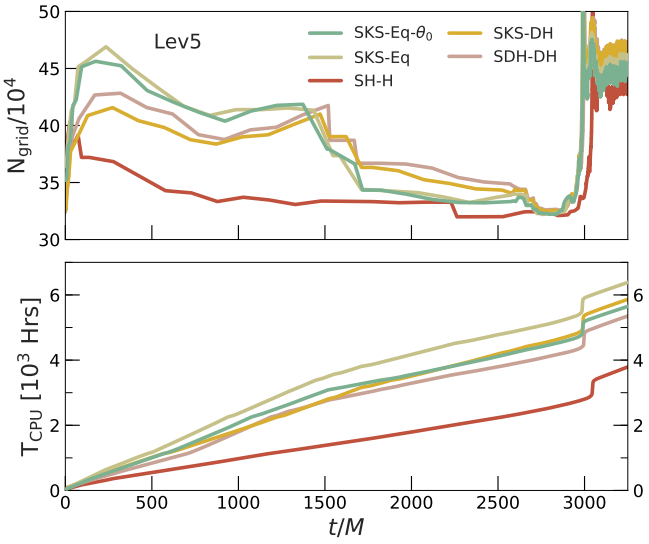

FIG. 8. Computational efficiency. The top panel shows the total number of collocation points versus time for several simulations running with the same AMR tolerance. The bottom panel shows the total CPU time as a function of the evolution time. Using SH-H initial data speeds up the evolution by about 33% compared to SKS-Eq-θ_0. All simulations are performed on the same machine with the same number of CPUs.

where $\tilde{\hbar}_1(f)$ is the Fourier transform of $\hbar_1(t)$, $\mathcal{R}[.]$ denotes the real part, $*$ denotes a complex conjugation, and f_{min} and f_{max} denote the relevant frequency range. f_{min} is chosen to be the GW frequency at a time $500M$ from the start (to exclude junk radiation) and f_{max} is chosen to be 8 times the merger frequency of the $\ell = m = 2$ mode.

We compute the mismatches as outlined in Appendix D of Ref. [58], where both polarizations are treated on an equal footing and the mismatch is minimized over shifts in time, initial binary phase, and polarization angle. We include all available modes ($\ell \leq 8, |m| \leq \ell$), when computing the strain

$$\hbar(\theta, \phi, t) = \sum_{\ell,m} {}^{-2}Y_{\ell m}(\theta, \phi)\ h_{\ell m}(t), \qquad (47)$$

where ${}^{-2}Y_{lm}(\theta, \phi)$ are the spin-weighted spherical harmonics, θ is the polar angle defined with respect to the initial orbital angular momentum direction and ϕ is the azimuthal angle in the source frame. We compute the mismatch for several different values of (θ, ϕ) (uniformly distributed in $\cos\theta$ and ϕ) and compare the median mismatches between different cases.

Figure 7 compares the median mismatches between waveforms from different initial data sets to the median mismatch between waveforms computed at different numerical resolutions. First, we note that the numerical resolution errors show reasonable convergence, as expected. Interestingly, we find that the differences between different initial data sets does not change significantly with resolution. We understand this as follows: Different initial data sets correspond to slightly different physical systems (i.e. they have different junk radiation and therefore slightly different orbital eccentricities and BH masses and spins, cf. Fig. 5 and Fig. 9) and this difference is independent of resolution. At low resolution, the differences due to different initial data sets are within the numerical resolution errors, as was found in Ref. [14]. However, contrary to the findings[5] of Ref. [14], as we go towards high resolution, the numerical resolution errors eventually go below the initial data differences. This suggests that the resolution is now high enough to differentiate between the initial data sets. These results also suggest that when very high accuracy is required, one should be concerned

[5] Note that Ref. [14] compares the phase and amplitude of the quadrupole mode ($\ell = 2$, $m = \pm 2$) to evaluate the errors between waveforms. Instead, we use the mismatch between the waveforms, including all available modes, to evaluate the errors. Also, Ref. [14] compares SKS-Eq-θ_0 initial data to CFMS (Conformally Flat Maximally Sliced) initial data, for an equal mass non-spinning BBH.

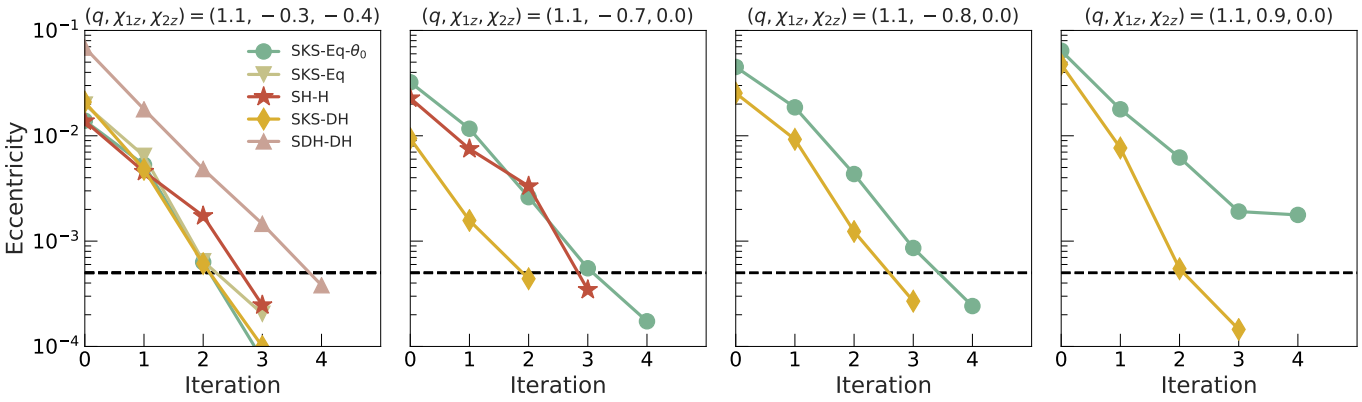

FIG. 9. Eccentricity reduction iterations for different initial data sets considered in this study. The parameters of the binary are shown in the text above each plot. We stop the iterations once the eccentricity reaches 5×10^{-4}; this cutoff is shown as a black dashed line.

with how well the initial data set represents the desired astrophysical system. Specifically, it is important to measure masses and spins after the junk radiation, and one must consider tuning initial data parameters to achieve desired "post-junk" parameters.

E. Simulation expense

As discussed at the beginning of Sec. V, the resolution of a simulation is determined by specifying an AMR error tolerance. For different simulations, the same AMR tolerance may result in a different number of collocation points and a different computational expense, since AMR chooses the number of collocation points based on the properties of the solution. Figure 8 shows the number of collocation points in the domain (top panel) and the total CPU time (bottom panel) for the different cases we consider, for a fixed AMR tolerance. For SH-H initial data, not only is the constraint violation during the junk radiation stage lower by an order of magnitude, this is achieved using 15% fewer collocation points and with a 33% speed-up compared to SKS-Eq-θ_0. This is another indication that evolutions of SH-H data contain fewer or smaller high-frequency features than for other initial data sets, so that AMR needs fewer collocation points to meet its error tolerance. These features can possibly be physical high-frequency oscillations associated with junk radiation, gauge oscillations, or gauge features that might manifest as sharper features in quasi-stationary metric functions near the horizons. We do not see significant differences in simulation expense between SKS-Eq-θ_0 and SDH-DH or SKS-DH initial data sets. While this speedup is shown for the specific case of $q = 1.1$, $\chi_{1z} = -0.3$, and $\chi_{2z} = -0.4$, we find similar improvements for more generic cases as well. However, since this improvement is largely due to lesser junk content, we expect speed-ups only in the initial stages of the evolution. For example, at times [6] $t > 1600M$ in Fig. 8, the number of grid points and the CPU-time per simulation time are comparable for SH-H and SKS-Eq-θ_0. This also implies that the speed advantage of SH-H will be less for longer simulations.

F. Constructing zero-eccentricity initial data

Unlike the Newtonian or post-Newtonian (PN) case, in full general relativity there is no analytic expression for the orbital parameters of two compact objects that yield a zero-eccentricity orbit. In order to achieve quasi-circular initial data, we adopt an iterative procedure as follows [54]: Start with an initial guess for orbital parameters $\mathbf{\Omega_0}$ and $\dot{a}_0$ (defined in Eq. 13), typically taken from PN. Construct initial data with these initial orbital parameters and evolve for ~ 2 orbits, compute the eccentricity from the binary orbit and update the initial orbital parameters. Repeat until the desired eccentricity is achieved.

Note that the eccentricity is measured over a few orbits of evolution, so that updating the initial orbital parameters effectively involves an extrapolation back in time to $t = 0$. When there is also a gauge transformation happening before or during the eccentricity measurement (cf. Sec. II C 1), this extrapolation can in principle be erroneous. Therefore, it is interesting to compare the eccentricity reduction procedure for the different initial data sets we construct. Particularly for SKS-DH and SDH-DH initial data sets, where there is no initial gauge transformation, we might expect improvements in eccentricity

[6] The outer boundary for these simulations is placed at a Euclidean radius of $800M$, so $1600M$ is approximately the light crossing time for the domain, at which point the junk radiation will have moved out of the domain.

reduction. Figure 9 shows the eccentricity reduction iterations for different initial data sets. While we see that SKS-DH reaches the desired eccentricity in fewer iterations than SKS-Eq-θ_0, we note that the initial guess from PN theory produces lower starting eccentricity for this case. In general, as the slopes of the curves do not differ significantly, we cannot conclusively say that the eccentricity reduction procedure improves when there is no gauge transformation. However, we find that SKS-DH is either better or the same as SKS-Eq-θ_0 for eccentricity reduction, for the cases we tested. Apart from SDH-DH initial data, all other initial data sets seem to perform at the same level as SKS-Eq-θ_0. For SDH-DH, while the rate of eccentricity reduction is the same, the initial guess from post-Newtonian theory produces higher eccentricity initial data. These results suggest that other approximations made in our eccentricity-reduction procedure have a larger influence than the effect of a time-dependent gauge transformation.

VI. CONCLUSION

In this paper, we introduce new ways to choose free data and new boundary conditions at excision surfaces, when constructing BBH initial data. Furthermore, we experiment with several initial gauge choices. We evolve these initial data sets and compare the waveforms, junk radiation, evolution of component parameters, constraint violations, simulation expense, and ease of constructing zero-eccentricity initial data for the different cases.

The initial data cases we compare include the following new features compared to the traditional "SKS" initial data (here called SKS-Eq-θ_0) used in past BBH simulations performed by the SpEC code:

- We introduce new boundary conditions that allow the initial-data numerical grid to extend inside (as opposed to on) the apparent horizons. Because the numerical grid for *evolution* must extend inside the apparent horizon, these new boundary conditions allow us to eliminate an extrapolation from the initial-data grid to the evolution grid. This reduces the initial constraint violations near the individual BH horizons by about 3 orders of magnitude. We denote the current implementation (SKS-Eq-θ_0) with only this change by SKS-Eq.

- We construct BBH initial data with free data given by a superposition of two Harmonic-Kerr single BHs as derived in Ref. [28]. The initial gauge is imposed by setting $\partial_t N$ and $\partial_t N^i$ according to the harmonic gauge condition. We denote this by SH-H.

- We construct BBH initial data with free data given by a superposition of two Damped-Harmonic single BHs as derived in Ref. [29]. The initial gauge is imposed by setting $\partial_t N$ and $\partial_t N^i$ according to the damped harmonic gauge condition. We denote this by SDH-DH.

- We also construct initial data identical to SKS-Eq above, except $\partial_t N$ and $\partial_t N^i$ are chosen according to the damped harmonic gauge condition as opposed to a quasiequilibrium condition. We denote this by SKS-DH.

Note that among these cases, we use the negative expansion boundary condition for all except SKS-Eq-θ_0 and we do a gauge transformation into the damped harmonic gauge over a time scale of $50M$ at the start of evolution for all except SDH-DH and SKS-DH (which already satisfy this gauge condition).

We compare these initial data sets by evolving a nonprecessing BBH system with mass ratio $q = 1.1$ and dimensionless spins $\chi_{1z} = -0.3$, $\chi_{2z} = -0.4$ along the orbital angular momentum direction. We compare the gravitational waves (extrapolated to spatial infinity) generated using the different initial data sets by computing the mismatches between them. We also compare these mismatches to the mismatches between waveforms evolved at different numerical resolution. As expected, the numerical resolution errors decrease as we go towards higher resolutions. However, we find that the mismatches between different initial data sets are approximately independent of resolution; we attribute this to the small physical differences between different initial data sets. These differences correspond to different amounts of junk radiation, and different parameters such as masses, spins, and orbital eccentricity. At low resolution, the initial data differences are below the numerical resolution errors. However, at high resolutions the numerical truncation error eventually drops below the initial data differences. Therefore, one must be careful to associate the waveform with the parameters (masses, spins, orbital eccentricity) measured after the junk radiation stage of the evolution rather than the parameters used to construct initial data.

A. The case for using SH-H initial data

By comparing the different initial data sets we conclude that SH-H initial data has the following benefits over the current implementation in SpEC (SKS-Eq-θ_0):

- The initial spurious junk radiation is much smaller.

- The junk radiation leaves the system sooner.

- The constraint violations during the junk radiation stage decrease by about an order of magnitude.

- The constraints have good convergence even during junk radiation. This suggests that the junk radiation is being resolved properly.

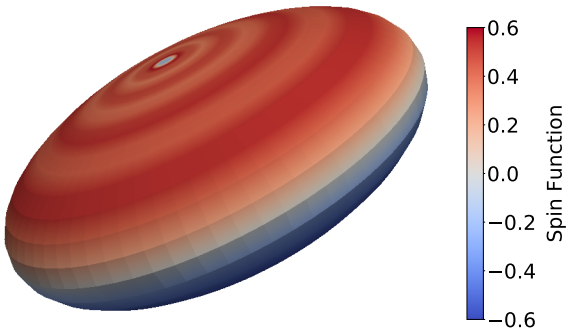

FIG. 10. Apparent horizon surface for a single BH with dimensionless spin $\chi = 0.9$ in the harmonic coordinates of Ref. [28]. The colors show the imaginary part of complex scalar curvature of the 2D horizon surface [59, 60]. The spin direction is along the poles. We note that the shape of the surface is compressed in the spin direction (much like a pancake), making it difficult to construct initial data. The ratio of the extents of the horizon between the spin direction and an orthogonal direction goes as $\sqrt{1-\chi^2}$, so this issue becomes more prominent at high spins. We currently can construct superposed harmonic initial data only for spins $\chi \leq 0.7$.

- The time variation in masses and spins during junk radiation is smaller by an order of magnitude.

- This improvement in constraints during junk radiation is achieved using 15% less collocation points in the domain. This leads to a remarkable 33% speed up in the total evolution time.

Because of these benefits, we recommend SH-H as the preferred choice for initial data, when possible. Unfortunately, we are currently able to construct SH-H initial data only for dimensionless spin magnitudes $\chi \leq 0.7$. At higher spins the single BH harmonic coordinates used for the construction of the free data in XCTS are too distorted (see Fig. 10), and the elliptic solver fails to converge. Therefore, we recommend that SH-H initial data be used for $\chi \leq 0.7$; otherwise, SKS-DH is our recommendation, since SKS-DH eliminates the need for extrapolation and for dynamical gauge changes, and it performs no worse than SKS-Eq-θ_0.

B. Outlook and future work

Having seen that SH-H initial data is superior to the current implementation in SpEC, it would be worthwhile to extend it to spins higher than $\chi = 0.7$. To overcome the problem with highly distorted horizons, one could use a coordinate map to make the horizons more spherical; this may violate the harmonic spatial gauge condition but will preserve harmonic time slicing. It would be interesting to see if such a map preserves the benefits of SH-H initial data.

Our tests on SH-H initial data suggest that even the junk radiation stage is convergent when using this initial data. Therefore, SH-H initial data allows us to study properties of junk radiation transients, such as their frequency content or how long they remain in the computational domain. For other initial data sets, the main obstacle for such a study is the prohibitively high resolution needed to fully resolve junk radiation.

ACKNOWLEDGMENTS

We thank Geoffrey Lovelace, Saul Teukolsky and Leo Stein for useful discussions. This work was supported in part by the Sherman Fairchild Foundation and NSF grants PHY-1404569, PHY-170212, and PHY-1708213 at Caltech. The simulations were performed on the Wheeler cluster at Caltech, which is supported by the Sherman Fairchild Foundation and Caltech.

[1] S. Khan, S. Husa, M. Hannam, F. Ohme, M. Prrer, X. Jimnez Forteza, and A. Boh, Phys. Rev. **D93**, 044007 (2016), arXiv:1508.07253 [gr-qc].
[2] M. Hannam, P. Schmidt, A. Bohé, L. Haegel, S. Husa, *et al.*, Phys. Rev. Lett. **113**, 151101 (2014), arXiv:1308.3271 [gr-qc].
[3] A. Bohé, L. Shao, A. Taracchini, A. Buonanno, S. Babak, I. W. Harry, I. Hinder, S. Ossokine, M. Pürrer, V. Raymond, T. Chu, H. Fong, P. Kumar, H. P. Pfeiffer, M. Boyle, D. A. Hemberger, L. E. Kidder, G. Lovelace, M. A. Scheel, and B. Szilágyi, Phys. Rev. D **95**, 044028 (2017), arXiv:1611.03703 [gr-qc].
[4] Y. Pan, A. Buonanno, A. Taracchini, L. E. Kidder, A. H. Mroué, H. P. Pfeiffer, M. A. Scheel, and B. Szilágyi, Phys. Rev. D **89**, 084006 (2013), arXiv:1307.6232 [gr-qc].
[5] A. Taracchini, A. Buonanno, Y. Pan, T. Hinderer, M. Boyle, D. A. Hemberger, L. E. Kidder, G. Lovelace, A. H. Mroue, H. P. Pfeiffer, M. A. Scheel, B. Szilágyi, N. W. Taylor, and A. Zenginoglu, Phys. Rev. D **89 (R)**, 061502 (2014), arXiv:1311.2544 [gr-qc].
[6] B. P. Abbott *et al.* (LIGO Scientific Collaboration, Virgo Collaboration), Phys. Rev. Lett. **116**, 061102 (2016), arXiv:1602.03837 [gr-qc].
[7] B. P. Abbott *et al.* (LIGO Scientific Collaboration, Virgo Collaboration), Phys. Rev. Lett. **116**, 241103 (2016), arXiv:1606.04855 [gr-qc].
[8] B. P. Abbott *et al.* (Virgo, LIGO Scientific), Astrophys. J. **851**, L35 (2017), arXiv:1711.05578 [astro-ph.HE].
[9] B. P. Abbott *et al.* (Virgo, LIGO Scientific), Phys. Rev. Lett. **119**, 141101 (2017), arXiv:1709.09660 [gr-qc].
[10] B. P. Abbott *et al.* (VIRGO, LIGO Scientific), Phys. Rev. Lett. **118**, 221101 (2017), arXiv:1706.01812 [gr-qc].
[11] J. Aasi *et al.* (LIGO Scientific Collaboration), Class. Quantum Grav. **32**, 074001 (2015), arXiv:1411.4547 [gr-

qc].
[12] B. P. Abbott *et al.* (LIGO Scientific Collaboration, Virgo Collaboration), Phys. Rev. Lett. **116**, 241102 (2016), arXiv:1602.03840 [gr-qc].
[13] B. P. Abbott *et al.* (LIGO Scientific Collaboration, Virgo Collaboration), Phys. Rev. Lett. **116**, 221101 (2016), arXiv:1602.03841 [gr-qc].
[14] B. Garcia, G. Lovelace, L. E. Kidder, M. Boyle, S. A. Teukolsky, M. A. Scheel, and B. Szilágyi, Phys. Rev. D **86**, 084054 (2012), arXiv:1206.2943 [gr-qc].
[15] `http://www.black-holes.org/SpEC.html`.
[16] J. W. York, Phys. Rev. Lett. **82**, 1350 (1999).
[17] H. P. Pfeiffer and J. W. York, Phys. Rev. D **67**, 044022 (2003).
[18] G. Lovelace, R. Owen, H. P. Pfeiffer, and T. Chu, Phys. Rev. D **78**, 084017 (2008).
[19] G. B. Cook and H. P. Pfeiffer, Phys. Rev. D **70**, 104016 (2004).
[20] L. Lindblom, M. A. Scheel, L. E. Kidder, R. Owen, and O. Rinne, Class. Quantum Grav. **23**, S447 (2006), arXiv:gr-qc/0512093v3 [gr-qc].
[21] H. Friedrich, Commun. Math. Phys. **100**, 525 (1985).
[22] D. Garfinkle, Phys. Rev. D **65**, 044029 (2002).
[23] F. Pretorius, Class. Quantum Grav. **22**, 425 (2005), gr-qc/0407110.
[24] M. A. Scheel, M. Boyle, T. Chu, L. E. Kidder, K. D. Matthews and H. P. Pfeiffer, Phys. Rev. D **79**, 024003 (2009), arXiv:gr-qc/0810.1767.
[25] L. Lindblom and B. Szilágyi, Phys. Rev. D **80**, 084019 (2009), arXiv:0904.4873.
[26] M. W. Choptuik and F. Pretorius, Phys. Rev. Lett. **104**, 111101 (2010), arXiv:0908.1780 [gr-qc].
[27] B. Szilágyi, L. Lindblom, and M. A. Scheel, Phys. Rev. D **80**, 124010 (2009), arXiv:0909.3557 [gr-qc].
[28] G. B. Cook and M. A. Scheel, Phys. Rev. D **56**, 4775 (1997).
[29] V. Varma and M. A. Scheel, Phys. Rev. **D98**, 084032 (2018), arXiv:1808.07490 [gr-qc].
[30] T. W. Baumgarte and S. L. Shapiro, Phys. Rev. D **59**, 024007 (1999), gr-qc/9810065.
[31] B. Brügmann, J. A. González, M. Hannam, S. Husa, U. Sperhake, and W. Tichy, Phys. Rev. D **77**, 024027 (2008), gr-qc/0610128.
[32] Y. Zlochower, J. Baker, M. Campanelli, and C. Lousto, Phys. Rev. D **72**, 024021 (2005), arXiv:gr-qc/0505055 [gr-qc].
[33] U. Sperhake, Phys. Rev. D **76**, 104015 (2007), gr-qc/0606079.
[34] D. Pollney, C. Reisswig, E. Schnetter, N. Dorband, and P. Diener, Phys. Rev. D **83**, 044045 (2011).
[35] F. Herrmann, I. Hinder, D. Shoemaker, and P. Laguna, Class. Quantum Grav. **24**, S33 (2007), gr-qc/0601026.
[36] L. Pekowsky, R. O'Shaughnessy, J. Healy, and D. Shoemaker, Phys. Rev. D **88**, 024040 (2013), arXiv:1304.3176 [gr-qc].
[37] S. Brandt and B. Brügmann, Phys. Rev. Lett. **78**, 3606 (1997).
[38] M. Shibata and T. Nakamura, Phys. Rev. D **52**, 5428 (1995).
[39] T. Nakamura, K. Oohara, and Y. Kojima, Prog. Theor. Phys. Suppl. **90**, 1 (1987).
[40] T. W. Baumgarte and S. L. Shapiro, *Numerical Relativity: Solving Einstein's Equations on the Computer* (Cambridge University Press, New York, 2010).
[41] H. P. Pfeiffer, J. Hyperbol. Differ. Eq. **2**, 497 (2005), gr-qc/0412002.
[42] G. Cook, Living Rev. Rel. **3** (2000), 5.
[43] G. Lovelace, *Numerical relativity data analysis. Proceedings, 2nd Meeting, NRDA 2008, Syracuse, USA, August 11-14, 2008*, Class. Quant. Grav. **26**, 114002 (2009), arXiv:0812.3132 [gr-qc].
[44] H. P. Pfeiffer, D. A. Brown, L. E. Kidder, L. Lindblom, G. Lovelace, and M. A. Scheel, Class. Quantum Grav. **24**, S59 (2007), gr-qc/0702106.
[45] G. B. Cook, Phys. Rev. D **65**, 084003 (2002).
[46] A. Ashtekar and B. Krishnan, Living Rev. Rel. **7** (2004), 10.
[47] O. Dreyer, B. Krishnan, D. Shoemaker, and E. Schnetter, Phys. Rev. D **67**, 024018 (2003).
[48] S. Ossokine, F. Foucart, H. P. Pfeiffer, M. Boyle, and B. Szilágyi, Class. Quantum Grav. **32**, 245010 (2015), arXiv:1506.01689 [gr-qc].
[49] L. T. Buchman, H. P. Pfeiffer, M. A. Scheel, and B. Szilágyi, Phys. Rev. D **86**, 084033 (2012), arXiv:1206.3015 [gr-qc].
[50] T. DeDonder, *La Gravifique Einsteinienne* (Gunthier-Villars, Paris, 1921).
[51] C. Lanczos, Phys. Z. **23**, 537 (1922).
[52] Y. Fourès-Bruhat, Acta Math. **88**, 141 (1952).
[53] A. E. Fischer and J. E. Marsden, Commun. Math. Phys. **28**, 1 (1972).
[54] A. Buonanno, L. E. Kidder, A. H. Mroué, H. P. Pfeiffer, and A. Taracchini, Phys. Rev. D **83**, 104034 (2011), arXiv:1012.1549 [gr-qc].
[55] H. P. Pfeiffer, L. E. Kidder, M. A. Scheel, and S. A. Teukolsky, Comput. Phys. Commun. **152**, 253 (2003), gr-qc/0202096.
[56] B. Szilágyi, Int. J. Mod. Phys. D **23**, 1430014 (2014), arXiv:1405.3693 [gr-qc].
[57] M. Boyle and A. H. Mroué, Phys. Rev. D **80**, 124045 (2009), arXiv:0905.3177 [gr-qc].
[58] J. Blackman, S. E. Field, M. A. Scheel, C. R. Galley, D. A. Hemberger, P. Schmidt, and R. Smith, Phys. Rev. **D95**, 104023 (2017), arXiv:1701.00550 [gr-qc].
[59] R. Owen, Phys. Rev. D **80**, 084012 (2009).
[60] R. Owen, J. Brink, Y. Chen, J. D. Kaplan, G. Lovelace, K. D. Matthews, D. A. Nichols, M. A. Scheel, F. Zhang, A. Zimmerman, and K. S. Thorne, Phys. Rev. Lett. **106**, 151101 (2011).